

Manifold-Aware Perturbations for Constrained Generative Modeling

Katherine Keegan¹ Lars Ruthotto¹

Abstract

Generative models have enjoyed widespread success in a variety of applications. However, they encounter inherent mathematical limitations in modeling distributions where samples are constrained by equalities, as is frequently the setting in scientific domains. In this work, we develop a computationally cheap, mathematically justified, and highly flexible distributional modification for combating known pitfalls in equality-constrained generative models. We propose perturbing the data distribution in a constraint-aware way such that the new distribution has support matching the ambient space dimension while still implicitly incorporating underlying manifold geometry. Through theoretical analyses and empirical evidence on several representative tasks, we illustrate that our approach consistently enables data distribution recovery and stable sampling with both diffusion models and normalizing flows.

1. Introduction

Generative models, such as Denoising Diffusion Probabilistic Models (DDPMs) (Ho et al., 2020), Score-Based Diffusion Models (SBDMs) (Song et al., 2021), and Normalizing Flows (NFs) (Papamakarios et al., 2021), have become ubiquitous for their ability to obtain high-quality samples from complex unknown distributions given finite data. These state-of-the-art paradigms model the data distribution p_0 as a pushforward of a tractable latent distribution p_T (often Gaussian) under some function f , which are then connected via the change of variables formula

$$p_T(x) = p_0(f^{-1}(x)) |\det J_f(x)|^{-1}. \quad (1)$$

The terminal Gaussian requirement ensures that the support of p_T in \mathbb{R}^d is *non-degenerate*, or fully d -dimensional. However, in many scientific tasks, samples $x \sim p_0$ also satisfy

¹Department of Mathematics, Emory University, Atlanta, Georgia, USA. Correspondence to: Katherine Keegan <katherine.emiri.keegan@emory.edu>.

some $h(x) = 0$, $h : \mathbb{R}^d \rightarrow \mathbb{R}^{d-m}$, often arising from physical laws or domain knowledge. The presence of an equality constraint with full-rank Jacobians means that p_0 lies on a m -dimensional manifold \mathcal{M} , making it a degenerate distribution embedded in \mathbb{R}^d . To be precise, p_0 is singular with respect to the d -dimensional Lebesgue measure.

Generative models under this framework require that the supports of p_0 and p_T have equal dimension. NFs rely on invertible transformations between p_0 and p_T in Equation (1). With a degenerate p_0 , the Jacobian determinant will be zero, leading to *exploding log-determinants*. Similarly, in diffusion models on manifold-supported p_0 , we encounter the issue of *score explosion*, where the score field guiding samples backwards in virtual time $t \in [0, T]$ explodes near the manifold as $t \rightarrow 0$, leading to sampling instability, unusable samples, and inaccurate generated distributions.

In this work, we propose a computationally cheap and mathematically motivated modification to p_0 , making it more amenable to training and sampling under any generative modeling paradigm. Our approach relies on (1) strategically noising data samples into the local normal bundle of \mathcal{M} to form a perturbed distribution p_σ , where σ parametrizes the perturbation strength, (2) training any unconstrained generative model, and then (3) projecting generated samples back to \mathcal{M} . We illustrate the utility of this approach on multiple datasets on both simple and complex manifolds. This work shows that our approach offers the following:

- **Perfect distribution recovery** for linear constraints
- **Bounded total variation** for nonlinear constraints
- **Guaranteed constraint adherence**
- **Bounded scores and non-zero Jacobian determinants** for diffusion and NF approaches, respectively, combating known pitfalls in equality-constrained generative model training and sampling arising from numerical instability
- **Improved or competitive** distributional fidelity

This paper shows that for equality-constrained distributions, p_σ is an attractive alternative target distribution: it removes the need for constraint adherence during sampling, avoids

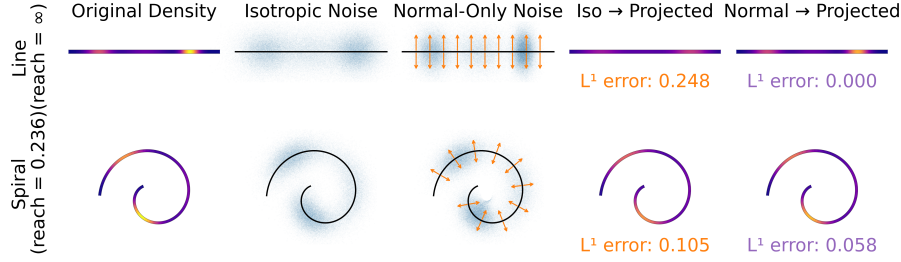


Figure 1. An illustration of our proposed manifold-aware perturbation and comparison to isotropic perturbations showing exact recovery for linear manifolds and lower error for the spiral dataset.

score or Jacobian determinant explosion, and offers mathematical guarantees in the induced projected distribution. We will publish our code upon acceptance.

2. Background and Related Literature

Degeneracy of $p_0(x)$ prevents the existence of a Lebesgue density and leads to several well-known pathologies in generative modeling. For instance, SBDMs assume differentiability of $\log p_0(x)$ in \mathbb{R}^d , and NFs require evaluation of log-densities under invertible transforms. Both become ill-defined or unbounded if $p_0(x)$ is singular with respect to the d -dimensional Lebesgue measure. In particular, the dimension mismatch of the distributions in Equation (1) prevents the existence of *any* invertible mapping between $p_0(x)$ and $p_T(x)$. In this work, we focus on the case where degeneracy is a result of being constrained by an m -dimensional manifold \mathcal{M} with full-rank Jacobians at all points $x \in \mathcal{M}$. The challenge of equality-constrained generative modeling has given rise to a variety of techniques, which may loosely be placed into the following two categories.

Modifying the underlying distribution. Many works directly modify the underlying distribution being learned by a generative model, with several techniques employing isotropic noising. This is present in well-known work on improving diffusion model effectiveness when data distributions lie on a lower-dimensional manifold (Song & Ermon, 2019). Similarly, SoftFlow (Kim et al., 2020) adds various levels of Gaussian noise to combat the dimension mismatch between p_0 and p_T during NF training and sampling. However, such isotropic approaches *immediately* risk distribution distortion if post-hoc projection is used to ensure constraint adherence, even for the simplest linear constraints.

Modifying the learning/sampling algorithm. Other works design novel constrained generative model families, develop constraint-aware training objectives, or enforce constraints during the sampling process. In the first case, many works focus on the case where the constraints define a Riemannian manifold. In this setting, one can make use of differential geometry and stochastic processes on manifolds

to define manifold-intrinsic SDEs, effectively constructing generative models which operate entirely on the constraint surface (Bortoli et al., 2022; Mathieu & Nickel, 2020). While elegantly ensuring constraint satisfaction, deriving such SDEs for general \mathcal{M} is nontrivial. Moreover, Riemannian generative models generally require many nontrivial manifold-aware computations throughout training and sampling, which can be computationally expensive and require careful and efficient implementation (Bortoli et al., 2022). Other recent developments in equality-constrained diffusion modeling include Projected Diffusion Models (PDMs) (Christopher et al., 2024), wherein the learned scores of an unconstrained model are iteratively projected to \mathcal{M} during sampling, and Physics-Informed Diffusion Models (PIDMs) (Bastek et al., 2024), in which constraint residuals are computed at $t = 0$ to form a physics-informed regularization loss term. However, these approaches necessitate high additional computational time: for PDM, this is needed during sampling, and for PIDM, the need to sample during training drastically affects training time, and neither approach offers guarantees of $p_0(x)$ recovery.

3. Method

In this paper, we present a novel contribution to works which aim to modify the underlying distribution being learned by a generative model. We propose an elegant distributional modification wherein p_0 is strategically distorted in a manifold-aware manner. In particular, we perturb $p_0(x)$ strictly in the normal direction(s) to \mathcal{M} at each x , implicitly incorporating underlying manifold geometry while setting up the modified distribution to have minimal error upon post-hoc manifold projection. Formally, this is as follows:

Definition 3.1 (p_σ). Draw $Z \sim p_0$ and $N|Z = z \sim \mathcal{N}(0, \sigma^2 I_{N_z \mathcal{M}})$, where $N_z \mathcal{M}$ denotes the normal space of \mathcal{M} at z . Set $X := Z + N \in \mathbb{R}^d$, and write $p_\sigma = \text{Law}(X)$. We refer to p_σ as the perturbed or lifted distribution associated with p_0 at noise scale $\sigma > 0$.

Operationally, one may implement the formation of p_σ by computing local Jacobians of the manifold surface around each sample $x \sim p_0$, using these to form bases for the

normal space, and perturbing each sample with Gaussian noise in the normal directions.

The reason for the intentionally anisotropic construction of p_σ is twofold: first, noising strictly in normal directions ensures that p_σ is no longer degenerate in the sense of its support in \mathbb{R}^d , vastly improving its compatibility with state-of-the-art (SOTA) out-of-the-box unconstrained generative modeling paradigms. Second, and unique to our work, anisotropic noising in this manner produces limited distortion and reduces artifacts in the induced distribution after projection, since tangential distortion along the manifold is minimal in curved regions and zero for linear regions.

To return to \mathcal{M} , we consider a (possibly multi-valued) nearest-point projection $\Pi : \mathbb{R}^d \rightarrow \mathcal{M}$, $\Pi(x) \in \arg \min_{z \in \mathcal{M}} \|x - z\|_2$, where ties are broken arbitrarily when the minimizer is not unique.

Algorithm 1 Procedure for forming the modified distribution p_σ and sampling under our approach.

Require: Constraint manifold \mathcal{M} , samples $x_0^i \sim p_0$
 1: Perturb each sample x_0^i strictly in normal direction of \mathcal{M} to obtain $x_\sigma^i \sim p_\sigma$
 2: Train generative model on $\{x_\sigma^i\}$ to model p_σ
 3: Sample $\hat{x}_\sigma^i \sim p_\sigma$
 4: Project \hat{x}_σ^i to \mathcal{M} using either analytic constraint projector or iterative minimization of $\arg \min_{z \in \mathcal{M}} \|x - z\|_2$

4. Error Analysis

The goal of this section is as follows: first, we discuss the nondegeneracy of p_σ and its advantages for generative modeling. Then, we prove that if constraints are linear, applying Π to samples from $p_\sigma(x)$ yields exactly the desired original intrinsic distribution. Finally, we bound the total variation (TV) distance on the manifold between the original distribution and the pushforward of p_σ upon nearest-point projection. We have constructed this section to be fairly self-contained so that a mathematically-inclined reader may read this section rigorously, while other readers can read the preceding section to understand our approach. For clarity, all variables and abbreviations are also described in the notation glossary provided in Appendix A.

Let $X : \Omega \rightarrow \mathbb{R}^d$ define a random variable on a probability space $(\Omega, \mathcal{F}, \mathbb{P})$. Its law is the measure $\mu(A) = \mathbb{P}(X \in A)$, with A being an element of the Borel σ -algebra $\mathcal{B}(\mathbb{R}^d)$. In order for the law μ to admit a density, one must select a reference measure ν on \mathbb{R}^d . If μ is absolutely continuous with respect to ν , then the Radon-Nikodym theorem guarantees the existence of a measurable function $p = \frac{d\mu}{d\nu}$ such that

$$\mu(A) = \int_A p(x) d\nu(x), A \in \mathcal{B}(\mathbb{R}^d).$$

Here, p is interpreted as the *density* of μ with respect to ν .

The standard reference measure for distributions over Euclidean space is the d -dimensional Lebesgue measure λ^d . A distribution μ is said to be *full-dimensional* if $\mu \ll \lambda^d$, in which case it admits a Lebesgue density $p(x)$. However, we say a law μ is *singular* if μ and λ^d are mutually singular, meaning that there exists a measurable set $A \subseteq \mathbb{R}^d$ such that $\mu(A) = 1$ and $\lambda^d(A) = 0$. Singular distributions arise naturally in many applications where data are constrained to lie on a lower-dimensional subset of the ambient space.

In this work, we refer to such singular laws as *degenerate distributions*. A canonical example of degeneracy arises when the support of μ is contained in an m -dimensional subset (e.g. a manifold \mathcal{M}) of \mathbb{R}^d with $m < d$. In this case, μ may admit a density with respect to an m -dimensional reference measure (e.g., the m -dimensional Hausdorff measure \mathcal{H}^m), but critically, *no density exists with respect to Lebesgue measure in the ambient space*. Such situations appear frequently in scientific domains where physical constraints restrict the degrees of freedom of the data.

To clarify the kinds of manifolds we study here, we briefly introduce some definitions from (Aamari et al., 2019).

Definition 4.1 (Medial Axis). The *medial axis*, denoted as $\Sigma(\mathcal{M})$, is the set of points $x \in \mathbb{R}^d$ where the nearest-point projection is multi-valued.

Definition 4.2 (Reach). The *reach* of a manifold \mathcal{M} is the minimal distance from any point on \mathcal{M} to $\Sigma(\mathcal{M})$.

Throughout our theoretical analyses, we assume \mathcal{M} to be **compact, \mathcal{C}^2 (twice-differentiable), and closed with positive reach**. In practice, some gentle smoothing on non-smooth regions (e.g. mesh edges) may be needed. However, the only requirement is the ability to compute local Jacobians on \mathcal{M} to extract normal vectors (where we assume Jacobians are full-rank at each $x \in \mathcal{M}$), so regularity may be relaxed from \mathcal{C}^2 to \mathcal{C}^1 in implementation. In fact, for mere implementation and not theoretical justification, \mathcal{M} need only be differentiable at the points where p_σ is nonzero.

We assume $p_0(x)$ lies on $\mathcal{M} : \{x \in \mathbb{R}^d : h(x) = 0\}$, where h is analytically known. In particular, p_0 is a density with respect to the m -dimensional Hausdorff measure \mathcal{H}^m , with law μ_0 where $d\mu_0 = p_0$. We assume p_0 to be Lipschitz on \mathcal{M} . We write the codimension of \mathcal{M} as $k = d - m$. We also assume p_0 to vary in all tangential directions to ensure that p_0 does not live on a proper submanifold of \mathcal{M} itself.

Theorem 4.3 (Geometric Non-degeneracy of p_σ). *The new distribution p_σ is not strictly supported on a lower-dimensional manifold.*

Proof. Adding Gaussian noise in $N_z \mathcal{M}$ at each $z \in \mathcal{M}$ thickens p_0 into a tubular distribution centered around \mathcal{M}

whose support contains all affine normal fibers $z + N_z \mathcal{M}$, yielding d -dimensional support. \square

We now discuss the law of the projected samples.

Definition 4.4 (Distribution of the Projected Samples). Define the pushforward of p_σ under Π as $\Pi_\# p_\sigma$. We will often refer to $\Pi_\# p_\sigma$ as \tilde{p}_σ for conciseness.

The nearest-point projection $\text{Proj}_{\mathcal{M}}(x)$ is unique if x lies in specific tubes around \mathcal{M} . Our bounds for nonlinear \mathcal{M} are executed entirely within such tubes and simply bound possible contributions from outside the tubes, and therefore the choice of tie-breaking in the selection of Π is arbitrary.

We first prove that $\Pi_\# p_\sigma$ and p_0 are exactly identical when h is linear (i.e. when \mathcal{M} has no curvature).

Theorem 4.5 (Perfect Recovery under Linear Constraints). *Let $h : \mathbb{R}^d \rightarrow \mathbb{R}^{d-m}$ be linear, e.g. $h(x) = Ax - b$, $A \in \mathbb{R}^{m \times d}$, $b \in \mathbb{R}^m$. Then, $p_0(x) = \tilde{p}_\sigma(x)$ for all $x \in \mathcal{M}$.*

Proof. Recall that p_σ is generated by adding noise strictly in $N_{x'} \mathcal{M}$ to samples x' to obtain ambient samples y . For linear \mathcal{M} , the nearest point from such y to \mathcal{M} is x' itself. \square

We remark that this is already immediately an advantage of our proposed approach compared to existing isotropic techniques: at any nonzero noising scale, isotropic noising followed by post-projection *immediately* induces distortion, as is seen in the linear manifold example in Figure 1.

We now bound the total variation (TV) for general nonlinear \mathcal{M} using the (intrinsic) TV as it is defined for probability densities with the \mathcal{H}^m measure on \mathcal{M} (Gibbs & Su, 2002):

$$\text{TV}(p, q) = \frac{1}{2} \int_{\mathcal{M}} |p(x) - q(x)| d\mathcal{H}^m(x).$$

Theorem 4.6 (Total Variation Bound). *The total variation distance (on \mathcal{M} , in \mathcal{H}^m) between \tilde{p}_σ and p_0 is bounded as*

$$\text{TV}(\tilde{p}_\sigma, p_0) \leq C_1 e^{-\frac{C_2 r^2}{\sigma^2}},$$

with $r < \text{reach}(\mathcal{M})$ and constants depending only on k .

Proof. See Appendix B. The idea is to construct a coupling between \tilde{p}_σ and p_0 . \square

Corollary 4.7 (Local Reach Bound). *Define $B_\rho(z) = \{z + n : \|n\| < \rho\}$. Let $\tau(\cdot)$ denote the pointwise reach function*

$$\tau(z) := \sup\{\rho > 0 : B_\rho(z) \text{ uniquely projects to } z\}.$$

Then, for each $z \in \mathcal{M}$,

$$D_\sigma(z) := \mathbb{E} [\text{dist}(z, \Pi(z + n))] \leq C_1 e^{-\frac{C_2 \tau(z)^2}{\sigma^2}}$$

and consequently

$$\text{TV}(\tilde{p}_\sigma, p_0) \leq 2L\sigma C_1 \int_{\mathcal{M}} e^{-C_2 \frac{\tau(z)^2}{\sigma^2}} d\mathcal{H}^m(z).$$

Proof. See Appendix B. The proof is similar to that of Theorem 4.6, but with a less restrictive global reach tube. \square

We also remark that Theorem 4.5 can also be understood as an immediate consequence of Theorem 4.6, as the reach of a linear manifold is infinity.

In practice, one may not need to worry about high curvature regions if probability mass is concentrated in low curvature regions. We find that $\sigma < \text{reach}(\mathcal{M})$ is a safe initial recommendation. We remark that the manifold reach is inversely proportional to its curvature, with (Aamari et al., 2019) being a good reference for further details. Ultimately, our theoretical analysis indicates that for applications where either (a) manifold global curvature is minimal, inducing high global or local reach, or (b) probability mass is estimated to be concentrated in regions of low local curvature, one can anticipate little distortion from learning and projecting p_σ .

Given the above results, one may reliably train any generative model (DDPM, SBDM, NF, etc.) to model p_σ , not p_0 , and project generated samples knowing that this procedure induces little to zero error. One can anticipate that generative modeling paradigms that operate in the manner of (1) will greatly benefit from our proposed approach, which directly targets the issue of dimension mismatch between the supports of the latent and the target distributions. Our experiments show both this minimal distortion as well as the expected improved sampling stability.

5. Numerical Experiments

We present experiments in order of ascending task complexity and scientific relevance. We first study distributions of 3-D points on 2-D manifolds (a plane, sphere, and mesh surface), followed by a 784-D image task and a 90-D application in protein backbone generation. Experimental configurations are delineated in Appendix C, and evaluation metrics are precisely described in Appendix D. For diffusion models, we implement PIDM, PDM, and DDPM on p_0 , with DDPM approaches also being used to model p_σ and an isotropically noised p_0 with the standard deviation matching the σ of the corresponding p_σ . We present NF results on the first two tasks to demonstrate improved Jacobian determinant stability, with p_σ , p_0 , and the isotropically noised p_0 modeled by RealNVP (Dinh et al., 2017) and Glow (Kingma & Dhariwal, 2018) architectures. We report sampling time in seconds and training time in seconds per batch. The label “ p_σ ” in figures refers to projected samples from a DDPM trained on p_σ .

5.1. Plane

We first discuss a simple distribution of 3-D points supported strictly on a 2-D plane. Precisely, samples x lie on

$$\mathcal{M}_{\text{plane}} := \{x \in \mathbb{R}^3 : Ax = b\},$$

where in our case, $A = [1, 2, 3]$ and $b = 0$.

	Method	Train time	Sampling time	COV \uparrow	JSD \downarrow	TVD \downarrow
Plane	PDM	0.0014	0.5173	0.8243	0.0715	0.2459
	PIDM	0.0025	0.1983	0.2256	0.4529	0.7998
	p_σ	0.0012	0.4426	0.8852	0.0442	0.1834
	DDPM	0.0012	0.1993	0.8787	0.0472	0.1844
	DDPM (proj.)	0.0012	0.1999	0.8772	0.0470	0.1833
	DDPM (proj., iso.)	0.0012	0.1999	0.8062	0.0793	0.2703
NFS	Glow (iso.)	0.0097	0.5474	0.9439	0.1111	0.3262
	Glow (p_σ , ours)	0.0097	0.5466	0.9491	0.1084	0.3198
	Glow (proj.)	0.0102	0.5488	0.9018	0.2704	0.5701
	Glow	0.0102	0.5460	0.8842	0.2782	0.5836
	RealNVP (iso.)	0.0118	0.1651	0.9368	0.0718	0.2461
	RealNVP (p_σ , ours)	0.0118	0.1649	0.9368	0.0690	0.2411
	RealNVP (proj.)	0.0114	0.1650	0.9000	0.3299	0.6567
	RealNVP	0.0114	0.1644	0.8842	0.3298	0.6576
	PDM	0.0014	0.3872	0.8273	0.0974	0.3092
	PIDM	0.0023	0.1984	0.1293	0.5998	0.9276
	p_σ	0.0012	0.2447	0.8853	0.0651	0.2382
	DDPM	0.0012	0.1989	0.8608	0.0805	0.2639
Sphere	DDPM (proj.)	0.0012	0.1993	0.8701	0.0739	0.2512
	DDPM (proj., iso.)	0.0012	0.1993	0.8700	0.0743	0.2579
	Glow	0.0097	0.3617	0.8170	0.3496	0.6783
	Glow (p_σ , ours)	0.0097	0.2835	0.8898	0.1009	0.3037
	Glow (proj.)	0.0097	0.3624	0.8877	0.1029	0.3033
	Glow (iso.)	0.0097	0.3624	0.8669	0.2928	0.5992
	RealNVP	0.0115	0.0842	0.8264	0.3158	0.6357
	RealNVP (p_σ , ours)	0.0115	0.0867	0.9075	0.0733	0.2398
	RealNVP (proj.)	0.0115	0.0846	0.7297	0.2984	0.6207
	RealNVP (iso.)	0.0115	0.0846	0.6143	0.3753	0.7089

Extrinsic metrics.

	Method	COV \uparrow	JSD \downarrow	TVD \downarrow
Plane	PDM	0.8243	0.0602	0.2267
	p_σ	0.8852	0.0336	0.1631
	DDPM (proj.)	0.8772	0.0363	0.1600
	DDPM (proj., iso.)	0.8062	0.0682	0.2577
	Glow (iso.)	0.8598	0.0742	0.2543
	Glow (p_σ , ours)	0.8551	0.0718	0.2529
Sphere	Glow (proj.)	0.6464	0.2200	0.5187
	RealNVP (iso.)	0.8928	0.0448	0.1878
	RealNVP (p_σ , ours)	0.8897	0.0429	0.1922
	RealNVP (proj.)	0.5688	0.2793	0.6019
	PDM	0.8311	0.0663	0.2566
	p_σ	0.8861	0.0364	0.1725
	DDPM (proj.)	0.8706	0.0459	0.1981
	DDPM (proj., iso.)	0.8727	0.0437	0.2047
	Glow (p_σ , ours)	0.8815	0.0707	0.2465
	Glow (proj.)	0.8775	0.0749	0.2636
	Glow (iso.)	0.6447	0.2508	0.5539
	RealNVP (p_σ , ours)	0.9019	0.0454	0.1787

Intrinsic metrics (using 2-D representations).

Table 1. Metrics for plane and sphere tasks at $\sigma = 0.05$. Among these experiments, learning p_σ always improves the sampled distribution compared to either learning p_0 or modifying the learning or sampling algorithms for the diffusion models. For NF approaches, we highlight the best-performing method within each architecture.

Due to computationally equivalent training objectives, it is expected that training time for p_σ , DDPM, projected DDPM (trained identically to DDPM), and PDM are close to identical. Table 1 includes the same metrics computed both extrinsically (all methods) and intrinsically (if applicable), where the latter is included for alignment with Section 4. We see that learning p_σ always leads to optimal or competitive distribution quality compared to other techniques. Figure 3 confirms this is consistent across various σ , and Figure 2 shows that learning p_σ indeed offers the expected benefits of reduced score and log-determinant magnitude.

5.2. Sphere

We then study the same distribution on a sphere, introducing global curvature while maintaining similar task complexity:

$$\mathcal{M}_{\text{sphere}} = \{x \in \mathbb{R}^3 : \|x\|_2 = 1\} \quad (2)$$

Table 1 shows that p_σ yields improved results across all metrics and is robust in providing competitive or improved performance within each paradigm. We also remark that in Figure 3, performance worsens as σ approaches 1.0. This aligns with results in Section 4, as $\text{reach}(\mathcal{M}_{\text{sphere}}) = 1.0$. This is notably not as dramatic for the plane task, as $\text{reach}(\mathcal{M}_{\text{plane}}) = \infty$, and any performance decrease is likely due to worsening data normalization with too-large σ .

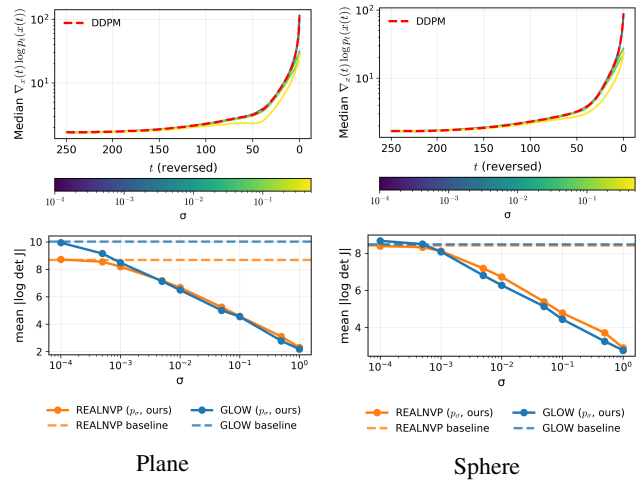


Figure 2. Sampling stability for plane and sphere tasks. We observe the expected reduction in score and Jacobian log-determinant magnitude across both tasks and generative modeling paradigms. We present similar results for the complex tasks in Appendix E.

5.3. Mesh

Here, we present results for a standard Gaussian supported strictly on the surface of the Stanford Bunny mesh (Stanford University Computer Graphics Laboratory). This experiment is inspired by results in (Elhag et al., 2023). We choose

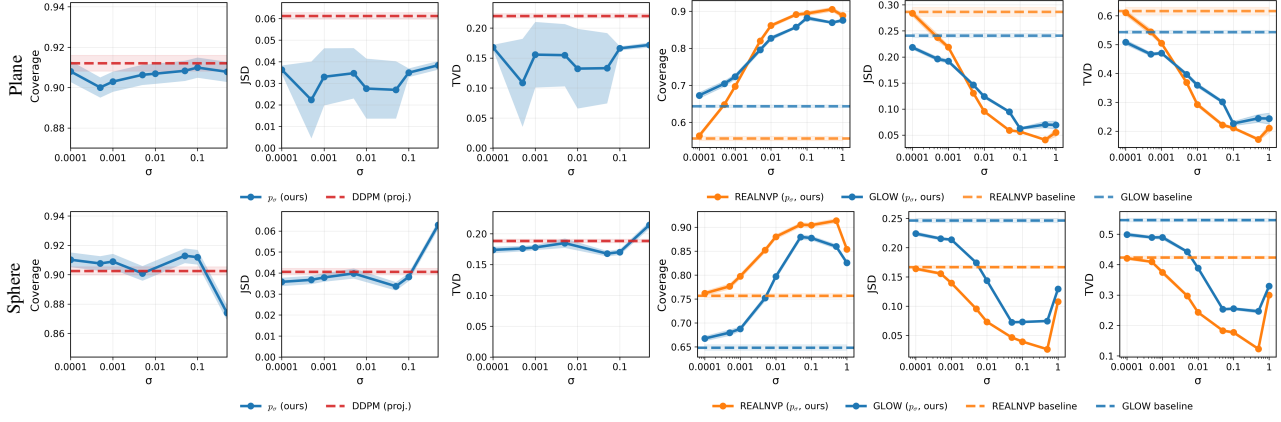


Figure 3. Metrics across varied σ for diffusion model and NF approaches on toy tasks. In all cases, learning p_σ consistently outperforms learning p_0 and post-projecting samples, with the expected possible performance decrease as $\sigma \rightarrow \text{reach}(\mathcal{M})$.

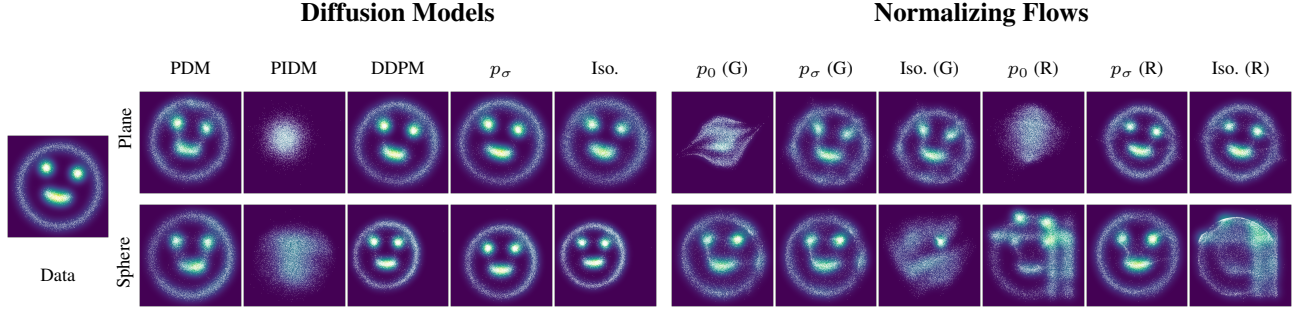


Figure 4. Image examples for plane and sphere tasks. In all cases, p_σ samples consistently visually outperform or are competitive against the other techniques. The label “(G)” refers to Glow and the label “(R)” refers to RealNVP.

this task as it maintains the same dimensionalities of the tasks in Sections 5.1-5.2 while introducing greater and more irregular local curvature.

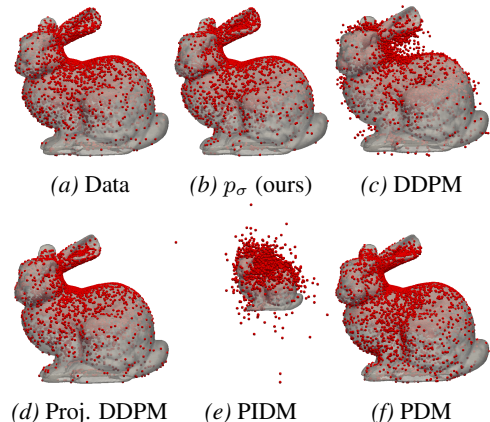


Figure 5. Mesh task samples. The projected p_σ samples are close to p_0 and do not risk off-manifold samples as others do.

In Figure 5, we see that the DDPM and PIDM approaches frequently produce off-manifold samples. Although projected DDPM samples visually align well with $p_0(x)$, they

consistently violate constraints prior to projection, suggesting that p_σ may be more reliable when both distributional fidelity and adherence to constraints are critical.

Method	Train time	Sampling time	COV \uparrow	JSD \downarrow	TVD \downarrow
PDM	0.0014	9.5618	0.8636	0.1827	0.4216
PIDM	0.0036	0.2201	0.2825	0.3351	0.6425
p_σ (ours)	0.0013	0.4234	0.8541	0.1468	0.3430
DDPM	0.0013	0.2340	0.7224	0.2617	0.4992
DDPM (proj.)	0.0013	0.2535	0.8643	0.1512	0.3563

Table 2. Mesh task metrics at $\sigma = 0.0005$. Learning p_σ is consistently competitive or an improvement upon other methods.

5.4. Image Generation with Total Flux Constraint

It is often the case in scientific inverse imaging tasks that the total flux of an image, or the sum of all pixel intensities, is constrained (Feng et al., 2024; The EHT Collaboration, 2019). To that end, we present a task of generating images with fixed total flux, where the sum of all pixel intensities is 100.0. We implement this task using 28×28 MNIST images (Deng, 2012), which may be represented as vectors $x \in \mathbb{R}^{784}$. This example is presented for its clear visual

notion of sample quality. The constraint manifold is thus

$$\mathcal{M}_{\text{flux}} := \left\{ x : \sum_{i=1}^{784} x_i = 100 \right\}.$$

Due to the challenge of histogram-based metrics in higher dimensions, we use learned embedding-based metrics inspired by the popular Frechét Inception Distance (Heusel et al., 2017), as well as an empirical JS-D over digit class distributions as inferred over a trained classifier. The precise procedure used to obtain these distances is described in thorough detail in Appendix D.

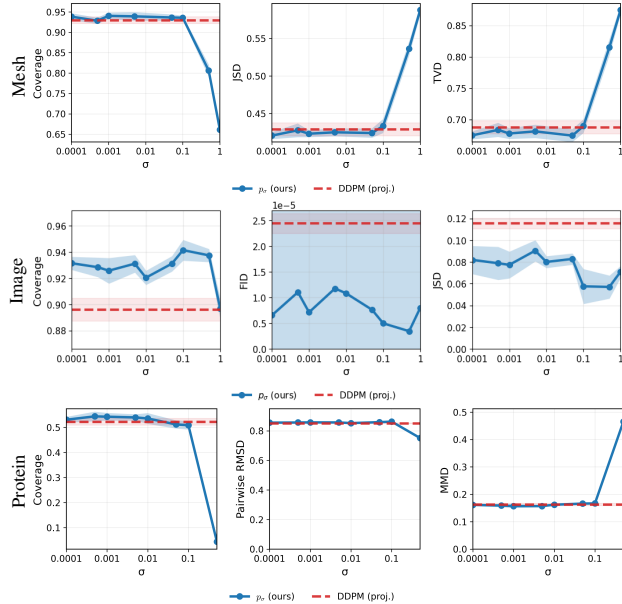


Figure 6. Metrics across varied σ on complex tasks. Learning p_σ consistently improves upon the projected DDPM baseline on all advanced problems.

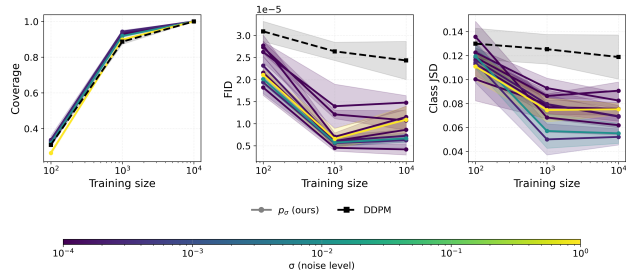


Figure 7. Performance improvement with respect to number of samples and σ on MNIST task. Learning p_σ at the tested σ levels consistently improves performance on all metrics, with an expected increase as the number of training samples increases.

In ablations against σ and the total training dataset size presented simultaneously in Figure 7, we see that our approach universally improves performance on the MNIST task on all

Method	Train time	Sampling time	COV \uparrow	FID \downarrow	Class JS-D \downarrow
p_σ (ours)	0.0081	4.7107	0.9040	8.311×10^{-6}	0.0634
DDPM	0.0080	9.3909	0.5127	6.736×10^{-4}	0.3315
DDPM	0.0080	4.7070	0.8453	2.411×10^{-5}	0.1124
PIDM	0.0096	4.7085	0.8043	2.477×10^{-5}	0.0886
DDPM (proj.)	0.0080	4.7081	0.8453	2.421×10^{-5}	0.1124

Table 3. MNIST metrics at $\sigma = 0.01$ with 10K training samples.

dataset sizes and choices of σ . We also remark that such results are consistent for fixed 10K training samples in Figure 6, wherein learning p_σ uniformly outperforms the projected DDPM baseline on all metrics.

5.5. Protein Backbone Generation

To demonstrate the effectiveness of our approach on real scientific data, we apply our technique to the generation of protein backbone fragments, which are the repeated N-CA-C atom structures present at the core of protein samples. Using generative AI to model the distribution of realistic protein backbones is an active area of research (Wu et al., 2024; Zhang et al., 2024; Xu et al., 2021), with downstream utility for prior-building in *de novo* and inverse design of proteins.

Protein backbone fragments abide by several underlying physical constraints: in particular, bond angles and lengths are rigidly constrained due to known chemical properties, imposing a geometric constraint on how the structures appear in 3-D space. Thus, applying out-of-the-box generative modeling techniques bears the risk of generating geometrically implausible structures. Moreover, existing state-of-the-art approaches to constraint-aware molecular structure generation, such as torsional diffusion (Jing et al., 2023), specifically cite protein generation, particularly in the backbone fragments, to be challenging due to the dimensionality of proteins. We do not claim to achieve SOTA performance against the many highly-tailored generative models constructed for computational biology applications. Rather, we present this as a highly realistic testbed for our approach with a complex constraint manifold and large data dimensionality, illustrating the potential of our technique for large-scale scientific generative modeling problems.

A single sample (a *fragment*) has size (# residues, # atoms, # coordinates), where the second dimension indexes the atom (N, CA, C) and the third dimension indexes the coordinates (x, y, z) in 3-D space for that atom. For each bond, we have a *bond length* and a *bond angle* constraint (the latter of which is taken over triplets of bonded atoms).

Let the coordinates of atom a in residue i be denoted by $x_{i,a} \in \mathbb{R}^3$. The full coordinate vector is then $x \in \mathbb{R}^D$ where $D = 9L$ (three atoms per residue, each with three coordinates, where L is the number of residues in the fragment).

We use fragments with lengths of 10 residues extracted from the CASP12 dataset as presented in SideChainNet (King & Koes, 2021; 2024), a dataset expanding the SOTA ProteinNet (AlQuraishi, 2019) with full backbone geometry information. We train on a subset of 20K fragments. Metrics are evaluated on sets of 1K samples.

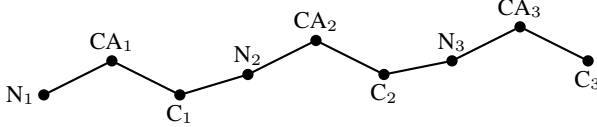


Figure 8. Backbone fragment with atom coordinates as generated variables. In our setting, a single data sample consists of L residues ($L = 3$ in this figure) with each residue made up of 3 backbone atoms (N, CA, C), each represented by (x, y, z) -coordinates.

Method	Train time	Sampling time	COV	Pairwise RMSD	MMD
p_σ (ours)	0.0036	1.9759	0.9490	1.6458	3.37×10^{-4}
DDPM	0.0035	1.4766	0.2910	0.7256	3.36 \times 10^{-4}
PDM	0.0037	206.7306	0.6330	1.4503	4.15×10^{-4}
DDPM (proj.)	0.0035	5.7733	0.5160	0.8407	3.36×10^{-4}
PIDM	0.3914	1.4180	0.3810	0.7776	3.36×10^{-4}

Table 4. Protein backbone fragment metrics at $\sigma = 0.001$.

In Table 4, we see that our approach outperforms other approaches on coverage and competitively on MMD with a bandwidth of 1.0. Moreover, as indicated by the Pairwise RMSD score (a metric of diversity amongst samples), this is accomplished without collapse to memorization of a single sample. While DDPM performs slightly better on the MMD metric, it violates constraints, and the post-projected DDPM samples have larger MMD. In comparison, the p_σ samples perform well on metrics of distributional fidelity and diversity with the added benefit of guaranteed constraint adherence (up to numerical optimization challenges) by construction of our approach. This, combined with the reduction in score magnitudes, indicates that our modified distribution may be strongly suitable for biological and molecular applications where strict geometric constraints are present.

6. Conclusions and Future Work

In this work, we demonstrated how a strategic pre- and post-processing step, in which we modify the underlying distribution being learned by a generative model, can circumvent common pitfalls in the generative modeling of manifold-supported distributions. Our technique offers automatic guarantees of both manifold adherence in samples through post-projection, which is not true for other approaches of similar computational requirements, as well as accurate distribution recovery according to intrinsic metrics on the manifold. We also present theoretical and experimental results which demonstrate that our approach either

improves upon or is competitive against SOTA generative modeling techniques while also frequently offering drastically reduced training or sampling time compared to other tailored constraint-aware approaches. We also observed in all experiments that our approach either outperforms other approaches according to evaluation metrics or performs competitively with drastically reduced sampling time, a known bottleneck in existing applications of generative models. Our examples on various data structures and task complexity demonstrate the utility of our approach in a wide variety of practical and scientific settings.

In this work, we experiment with learning p_σ using multiple popular generative modeling techniques, specifically those falling under diffusion model and NF paradigms. However, our approach is highly flexible and not restricted to these training parameterizations; our results support the claim that learning and projecting p_σ is a much more stable and reliable way to apply generative models to constrained tasks regardless of the chosen technique for distribution modeling.

One can also consider our approach applied to diffusion models from an SDE perspective. So far, we have essentially modified the forward process to apply 1. anisotropic noise first to push points off \mathcal{M} and then 2. the usual isotropic noising to allow standard training. One could extend our approach to replace the $\beta(t)$ noise variance schedule in the diffusion model forward process with a spatially-dependent $\beta(x, t)$ (or perhaps $\beta(x, t, \mathcal{M})$). Future work may consider a continuous interpolation between isotropic and our anisotropic noising in the diffusion model SDEs.

Our theoretical analyses demonstrate that the error between $p_\sigma(x)$ and $p_0(x)$ is dominated by manifold curvature via the reach. Future work may investigate defining a *spatially-dependent* σ_x , which can be larger in linear regions and reduced in regions of greater, more irregular curvature. Expanding p_σ to be aware of second-order manifold information through curvature is a natural next step for combating challenges in sampling from degenerate distributions.

Acknowledgements

This material is based upon work supported by the U.S. Department of Energy, Office of Science, Office of Advanced Scientific Computing Research, Department of Energy Computational Science Graduate Fellowship under Award Number(s) DE-SC0023112. The authors also acknowledge support from NSF award DMS 2038118.

Impact Statement

This paper presents work with the broader goal of aligning AI for domain science use cases, where ensuring mathematical guarantees and adherence with known constraints is

particularly crucial. In many of these applications, ensuring synergy between known laws originating from domain sciences and data-driven techniques in generative AI is crucial for meaningful implementation in actual science workflows. As such, the potential societal consequences of our work match those of general AI4Science endeavors.

References

Aamari, E., Kim, J., Chazal, F., Michel, B., Rinaldo, A., and Wasserman, L. Estimating the Reach of a Manifold, April 2019. URL <http://arxiv.org/abs/1705.04565>. arXiv:1705.04565 [math].

AlQuraishi, M. ProteinNet: a standardized data set for machine learning of protein structure. *BMC Bioinformatics*, 20(1):311, June 2019. ISSN 1471-2105. doi: 10.1186/s12859-019-2932-0. URL <https://doi.org/10.1186/s12859-019-2932-0>.

Bastek, J.-H., Sun, W., and Kochmann, D. M. Physics-Informed Diffusion Models, May 2024. URL <http://arxiv.org/abs/2403.14404>. arXiv:2403.14404.

Benny, Y., Galanti, T., Benaim, S., and Wolf, L. Evaluation Metrics for Conditional Image Generation. *International Journal of Computer Vision*, 129(5):1712–1731, May 2021. ISSN 0920-5691, 1573-1405. doi: 10.1007/s11263-020-01424-w. URL <http://arxiv.org/abs/2004.12361>. arXiv:2004.12361 [cs].

Bortoli, V. D. Convergence of denoising diffusion models under the manifold hypothesis, May 2023. URL <http://arxiv.org/abs/2208.05314>. arXiv:2208.05314 [stat].

Bortoli, V. D., Mathieu, E., Hutchinson, M., Thornton, J., Teh, Y. W., and Doucet, A. Riemannian Score-Based Generative Modelling, November 2022. URL <http://arxiv.org/abs/2202.02763>. arXiv:2202.02763 [cs].

Chazal, F., Cohen-Steiner, D., and Mérigot, Q. Boundary Measures for Geometric Inference. *Foundations of Computational Mathematics*, 10(2):221–240, April 2010. ISSN 1615-3383. doi: 10.1007/s10208-009-9056-2. URL <https://doi.org/10.1007/s10208-009-9056-2>.

Christopher, J. K., Baek, S., and Fioretto, F. Constrained Synthesis with Projected Diffusion Models, November 2024. URL <http://arxiv.org/abs/2402.03559>. arXiv:2402.03559 [cs].

Daskalakis, C., Chiesa, A., and Zhu, Z. Probability and computation: Lecture 3. <https://people.csail.mit.edu/costis/6896sp11/lec3s.pdf>,

February 2011. Lecture notes for 6.896: Probability and Computation, Spring 2011.

Deng, L. The MNIST Database of Handwritten Digit Images for Machine Learning Research [Best of the Web]. *IEEE Signal Processing Magazine*, 29(6):141–142, November 2012. ISSN 1558-0792. doi: 10.1109/MSP.2012.2211477. URL <https://ieeexplore.ieee.org/document/6296535>.

Dinh, L., Sohl-Dickstein, J., and Bengio, S. Density estimation using Real NVP, February 2017. URL <http://arxiv.org/abs/1605.08803>. arXiv:1605.08803 [cs].

Elhag, A. A. A., Wang, Y., Susskind, J. M., and Bautista, M. Á. Manifold Diffusion Fields. October 2023. URL <https://openreview.net/forum?id=BZtEthuXRF>.

Evans, L. C. and Gariepy, R. F. *Measure Theory and Fine Properties of Functions, Revised Edition*. Chapman and Hall/CRC, New York, April 2015. ISBN 9780429161483. doi: 10.1201/b18333.

Feng, B. T., Baptista, R., and Bouman, K. L. Neural Approximate Mirror Maps for Constrained Diffusion Models, June 2024. URL <http://arxiv.org/abs/2406.12816>. arXiv:2406.12816.

Gibbs, A. L. and Su, F. E. On Choosing and Bounding Probability Metrics. *International Statistical Review / Revue Internationale de Statistique*, 70(3):419–435, 2002. ISSN 0306-7734. doi: 10.2307/1403865. URL <https://www.jstor.org/stable/1403865>.

Heusel, M., Ramsauer, H., Unterthiner, T., Nessler, B., and Hochreiter, S. GANs Trained by a Two Time-Scale Update Rule Converge to a Local Nash Equilibrium. In *Advances in Neural Information Processing Systems*, volume 30. Curran Associates, Inc., 2017. URL https://proceedings.neurips.cc/paper_files/paper/2017/hash/8a1d694707eb0fefe65871369074926d-Abstract.html.

Ho, J., Jain, A., and Abbeel, P. Denoising Diffusion Probabilistic Models, December 2020. URL <http://arxiv.org/abs/2006.11239>. arXiv:2006.11239.

Huang, C.-W., Aghajohari, M., Bose, A. J., Panangaden, P., and Courville, A. Riemannian Diffusion Models, August 2022. URL <http://arxiv.org/abs/2208.07949>. arXiv:2208.07949 [cs].

Jayasumana, S., Ramalingam, S., Veit, A., Glasner, D., Chakrabarti, A., and Kumar, S. Rethinking FID: Towards a Better Evaluation Metric for Image Generation. In *2024 IEEE/CVF Conference on Computer*

Vision and Pattern Recognition (CVPR), pp. 9307–9315, June 2024. doi: 10.1109/CVPR52733.2024.00889. URL <https://ieeexplore.ieee.org/document/10656361>. ISSN: 2575-7075.

Jing, B., Corso, G., Chang, J., Barzilay, R., and Jaakkola, T. Torsional Diffusion for Molecular Conformer Generation, March 2023. URL <http://arxiv.org/abs/2206.01729>. arXiv:2206.01729 [physics].

Kim, H., Lee, H., Kang, W. H., Lee, J. Y., and Kim, N. S. SoftFlow: Probabilistic Framework for Normalizing Flow on Manifolds, November 2020. URL <http://arxiv.org/abs/2006.04604>. arXiv:2006.04604 [cs].

King, J. E. and Koes, D. R. SidechainNet: An All-Atom Protein Structure Dataset for Machine Learning. *Proteins*, 89(11):1489–1496, November 2021. ISSN 0887-3585. doi: 10.1002/prot.26169. URL <https://www.ncbi.nlm.nih.gov/pmc/articles/PMC8492522/>.

King, J. E. and Koes, D. R. Interpreting forces as deep learning gradients improves quality of predicted protein structures. *Biophysical Journal*, 123(17):2730–2739, September 2024. ISSN 1542-0086. doi: 10.1016/j.bpj.2023.12.011.

Kingma, D. P. and Dhariwal, P. Glow: Generative Flow with Invertible 1x1 Convolutions, July 2018. URL <http://arxiv.org/abs/1807.03039>. arXiv:1807.03039 [stat].

Lecun, Y., Bottou, L., Bengio, Y., and Haffner, P. Gradient-based learning applied to document recognition. *Proceedings of the IEEE*, 86(11):2278–2324, November 1998. ISSN 1558-2256. doi: 10.1109/5.726791. URL <https://ieeexplore.ieee.org/document/726791>.

Leobacher, G. and Steinicke, A. Existence, Uniqueness and Regularity of the Projection onto Differentiable Manifolds, February 2020. URL <http://arxiv.org/abs/1811.10578>. arXiv:1811.10578 [math].

Mathieu, E. and Nickel, M. Riemannian Continuous Normalizing Flows, December 2020. URL <http://arxiv.org/abs/2006.10605>. arXiv:2006.10605 [stat].

Papamakarios, G., Nalisnick, E., Rezende, D. J., Mohamed, S., and Lakshminarayanan, B. Normalizing Flows for Probabilistic Modeling and Inference, April 2021. URL <http://arxiv.org/abs/1912.02762>. arXiv:1912.02762 [stat].

Roch, S. Chapter 4: Coupling. <https://people.math.wisc.edu/~roch/mdp/roch-mdp-chap4.pdf>, 2023. In *Modern Discrete Probability: An Essential Toolkit*. Version: December 20, 2023.

Song, Y. and Ermon, S. Generative modeling by estimating gradients of the data distribution. In *Proceedings of the 33rd International Conference on Neural Information Processing Systems*, number 1067, pp. 11918–11930. Curran Associates Inc., Red Hook, NY, USA, December 2019. URL <https://dl.acm.org/doi/10.5555/3454287.3455354>.

Song, Y., Sohl-Dickstein, J., Kingma, D. P., Kumar, A., Ermon, S., and Poole, B. Score-Based Generative Modeling through Stochastic Differential Equations, February 2021. URL <http://arxiv.org/abs/2011.13456>. arXiv:2011.13456.

Stanford University Computer Graphics Laboratory. Stanford bunny. <https://graphics.stanford.edu/data/3Dscanrep/>. The Stanford 3D Scanning Repository.

The EHT Collaboration. First m87 event horizon telescope results. iv. imaging the central supermassive black hole. *ApJL*, 875:4, 2019. URL <https://iopscience.iop.org/article/10.3847/2041-8213/ab0e85>.

Wu, K. E., Yang, K. K., van den Berg, R., Alamdari, S., Zou, J. Y., Lu, A. X., and Amini, A. P. Protein structure generation via folding diffusion. *Nature Communications*, 15(1):1059, February 2024. ISSN 2041-1723. doi: 10.1038/s41467-024-45051-2. URL <https://www.nature.com/articles/s41467-024-45051-2>.

Xu, Y.-C., ShangGuan, T.-J., Ding, X.-M., and Cheung, N. J. Accurate prediction of protein torsion angles using evolutionary signatures and recurrent neural network. *Scientific Reports*, 11(1):21033, October 2021. ISSN 2045-2322. doi: 10.1038/s41598-021-00477-2. URL <https://www.nature.com/articles/s41598-021-00477-2>.

Zhang, Y., Liu, Y., Ma, Z., Li, M., Xu, C., and Gong, H. Improving diffusion-based protein backbone generation with global-geometry-aware latent encoding, October 2024. URL <https://www.biorxiv.org/content/10.1101/2024.10.05.616664v1>.

A. Notation Glossary

Symbol	Description
<i>Spaces and Manifolds</i>	
\mathbb{R}^d	Ambient space (dimension d)
\mathcal{M}	m -dimensional constraint manifold embedded in \mathbb{R}^d
m	Intrinsic dimension of \mathcal{M}
$k = d - m$	Codimension of \mathcal{M}
$T_x\mathcal{M}$	Tangent space to \mathcal{M} at point x
$N_x\mathcal{M}$	Normal space to \mathcal{M} at point x
$\text{reach}(\mathcal{M})$	Global reach of manifold \mathcal{M}
$\tau(z)$	Pointwise reach function at $z \in \mathcal{M}$
$r < \text{reach}(\mathcal{M})$	Radius of reach tube $T_r(\mathcal{M})$
<i>Constraints</i>	
$h : \mathbb{R}^d \rightarrow \mathbb{R}^m$	Constraint function defining $\mathcal{M} = \{x : h(x) = 0\}$
$J_h(x)$	Jacobian of constraint function at x
<i>Distributions and Measures</i>	
$p_0(x)$	Original data distribution on \mathcal{M}
$p_\sigma(x)$	Perturbed (lifted) distribution in \mathbb{R}^d
$\tilde{p}_\sigma(x)$	Projected distribution $\Pi_\# p_\sigma$ on \mathcal{M}
$p_T(x)$	Terminal/latent distribution (typically $\mathcal{N}(0, I)$)
μ	Probability measure/law
λ^d	d -dimensional Lebesgue measure
\mathcal{H}^m	m -dimensional Hausdorff measure
<i>Random Variables</i>	
Z	Random variable with law p_0 on \mathcal{M}
$N Z = z$	Conditional Gaussian noise in $N_z\mathcal{M}$
$X = Z + N$	Lifted random variable with law p_σ
$Y = \Pi(X)$	Projected random variable with law \tilde{p}_σ
<i>Operators and Functions</i>	
$\Pi : \mathbb{R}^d \rightarrow \mathcal{M}$	Nearest-point projection onto \mathcal{M}
<i>Hyperparameters</i>	
σ	Noise scale for perturbation
$t \in [0, T]$	Virtual time for diffusion process
T	Terminal time (typically $T = 250$ in experiments)
<i>Metrics</i>	
$\text{TV}(p, q)$	Total variation distance: $\frac{1}{2} \int_{\mathcal{M}} p(x) - q(x) d\mathcal{H}^m(x)$
$\text{JSD}(p\ q)$	Jensen-Shannon divergence
COV	Coverage metric
FID	Fréchet Inception Distance.
RMSD	Root mean square deviation
MMD	Maximum Mean Discrepancy

Table 5. Summary of notation used throughout this paper.

We note that while we use the term ‘‘FID’’ to refer to the popular metric for image generation analysis, our implementation is an approximation using a LeNet classifier instead of the Inception-V3 architecture standard for FID. The precise details of our implementation are described in Appendix D.

B. Theory

Lemma B.1 (\mathcal{C}^1 -ness of Π on $\mathbb{R}^d \setminus \Sigma(\mathcal{M})$). *If $\mathcal{M} \in \mathcal{C}^2$, then $\Pi(x) : \mathbb{R}^d \setminus \Sigma(\mathcal{M}) \rightarrow \mathcal{M} \in \mathcal{C}^1$. Moreover, as \mathcal{C}^1 implies being locally Lipschitz, Π is locally Lipschitz on this domain.*

Proof. This is a direct consequence of the main result in (Leobacher & Steinicke, 2020), which states that for \mathcal{C}^k -submanifolds with $k \geq 2$, Π is \mathcal{C}^{k-1} on the maximal open domain where Π is uniquely valued. \square

Theorem B.2 (Difference of $\text{Proj}_{\mathcal{M}}$ and Π). *Under the assumptions of \mathcal{M} in this paper, $\lambda^d(\Sigma(\mathcal{M})) = 0$.*

Proof. By (Chazal et al., 2010), $\Sigma(\mathcal{M})$ has \mathcal{H}^d -measure zero, and as \mathcal{H}^d and λ^d agree by Chapter 2.2 in (Evans & Gariepy, 2015), $\lambda^d(\Sigma(\mathcal{M})) = 0$. \square

Lemma B.3 (Gaussian Tails of p_σ Outside of $T_r(\mathcal{M})$). *We have*

$$\int_{\mathbb{R}^d \setminus T_r(\mathcal{M})} p_\sigma(x) dx \leq C_1 e^{-C_2 \frac{r^2}{\sigma^2}}, \quad C_1 = 2^{\frac{(d-m)}{2}}, \quad C_2 = \frac{1}{4}.$$

Proof. We have

$$\int_{\mathbb{R}^d \setminus T_r(\mathcal{M})} p_\sigma(x) dx = \mathbb{P}(X \in \mathbb{R}^d \setminus T_r(\mathcal{M})).$$

Recall that the procedure for forming p_σ yields $X = Z + N$ with N conditional on $Z = z$ being sampled from $\mathcal{N}(0, \sigma^2 I_{N_z \mathcal{M}})$, note that for any $(Z, N) = (z, n)$, we have

$$z + n \in T_r(\mathcal{M}) \Leftrightarrow \|n\| < r.$$

Thus, for any particular $X = Z + N$, we have

$$\{X \notin T_r(\mathcal{M})\} = \{\|N\| \geq r\}.$$

Therefore, the remainder of the proof amounts to simply identifying an upper bound on the tail probability of the k -dimensional Gaussian N .

It is known that the squared norm of N follows a χ^2 distribution with k degrees of freedom:

$$\frac{\|N\|^2}{\sigma^2} \sim \chi_k^2.$$

This gives

$$\mathbb{P}(\|N\| \geq r) = \mathbb{P}\left(\frac{\|N\|^2}{\sigma^2} \geq \frac{r^2}{\sigma^2}\right) = \mathbb{P}(U \geq u),$$

in which $U \sim \chi_k^2$ and $u := \frac{r^2}{\sigma^2}$.

The moment generating function for a random variable following a χ_k^2 distribution is

$$\mathbb{E}[e^{\lambda U}] = (1 - 2\lambda)^{-\frac{k}{2}}.$$

Let $\lambda = \frac{1}{4} \in (0, \frac{1}{2})$. Then

$$(1 - 2\lambda)^{-\frac{k}{2}} = \left(1 - \frac{1}{2}\right)^{-\frac{k}{2}} = 2^{\frac{k}{2}}$$

and

$$\begin{aligned}
 \mathbb{P}(U \geq u) &= \mathbb{P}(e^{\lambda U} \geq e^{\lambda u}) \\
 &\leq e^{-\lambda u} \mathbb{E}[e^{\lambda U}] \text{ by Markov's inequality} \\
 &\leq e^{-\frac{1}{4}u} 2^{\frac{k}{2}} \\
 &= 2^{\frac{k}{2}} e^{-\frac{1}{4}\frac{u^2}{\sigma^2}}.
 \end{aligned}$$

□

Proof of Theorem 4.6. Recall that p_0 is a density on $(\mathcal{M}, \mathcal{H}^m)$, and that p_σ is obtained by adding Gaussian noise in the normal bundle. We first construct an explicit coupling (Daskalakis et al., 2011; Roch, 2023) between $p_0 \mathcal{H}^m$ and $\tilde{p}_\sigma \mathcal{H}^m$.

Let Z be a \mathcal{M} -supported random variable with law $p_0 \mathcal{H}^m$, i.e.

$$\mathbb{P}(Z \in A) = \int_A p_0(z) d\mathcal{H}^m(z), A \subset \mathcal{M}.$$

Conditionally on $Z = z$, draw Gaussian noise vector $N \in N_z \mathcal{M}$, $N \mid Z = z \sim \mathcal{N}(0, \sigma^2 I_{N_z \mathcal{M}})$, and set

$$X := Z + N \in \mathbb{R}^d, Y := \Pi(x) \in \mathcal{M}.$$

By construction, the law of Z is exactly $p_0 \mathcal{H}^m$. Moreover, the law of X is precisely the lifted distribution $p_\sigma(x)dx$: for any Borel set $B \subset \mathbb{R}^d$,

$$\mathbb{P}(X \in B) = \int_{\mathcal{M}} \mathbb{P}(Z + N \in B \mid Z = z) p_0(z) d\mathcal{H}^m(z) = \int_B p_\sigma(x) dx.$$

Since $Y = \Pi(x)$, its law is the pushforward of $p_\sigma(x)dx$ under Π , i.e.

$$\begin{aligned}
 \mathbb{P}(Y \in A) &= \mathbb{P}(X \in \Pi^{-1}(A)) \\
 &= \int_{\Pi^{-1}(A)} p_\sigma(x) dx \\
 &= (\Pi_\# p_\sigma)(A) \\
 &= \int_A \tilde{p}_\sigma(y) \mathcal{H}^m(y),
 \end{aligned}$$

so Y has law $\tilde{p}_\sigma \mathcal{H}^m$,

Therefore, the joint law of (Z, Y) , is a coupling of the probability measures $p_0 \mathcal{H}^m$ and $\tilde{p}_\sigma \mathcal{H}^m$ on \mathcal{M} .

It is standard (Daskalakis et al., 2011; Roch, 2023) that for any coupling (U, V) of μ and ν ,

$$\|\mu - \nu\|_{\text{TV}} \leq \mathbb{P}(U \neq V).$$

In our setting,

$$\text{TV}(\tilde{p}_\sigma, p_0) = \|\tilde{p}_\sigma \mathcal{H}^m - p_0 \mathcal{H}^m\|_{\text{TV}} \leq \mathbb{P}(Z \neq Y).$$

We now bound $\mathbb{P}(Z \neq Y)$ using the reach of \mathcal{M} . Fix any radius $0 < r < \text{reach}(\mathcal{M})$ and recall that for \mathcal{C}^2 embedded manifolds, an equivalent characterization of the reach is that for all $z \in \mathcal{M}$ and all $n \in N_z \mathcal{M}$ with $\|n\| < r$, the point $x = z + n$ has z as its unique nearest point on \mathcal{M} , hence $\Pi(z + n) = z$. In particular, if $\|N\| < r$ then $X = Z + N$ lies in the reach tube and

$$Y = \Pi(X) = \Pi(Z + N) = Z.$$

Therefore,

$$\{Z \neq Y\} \subseteq \{\|N\| \geq r\},$$

and hence

$$\mathbb{P}(Z \neq Y) \leq \mathbb{P}(\|N\| \geq r).$$

By construction, N is a k -dimensional Gaussian in the normal space with law $\mathcal{N}(0, \sigma^2 I_k)$. The event $\{\|N\| \geq r\}$ is exactly the event that X lies outside the tubular neighborhood of radius r . In particular,

$$\mathbb{P}(\|N\| \geq r) = \int_{\mathbb{R}^d \setminus T_r(\mathcal{M})} p_\sigma(x) dx.$$

Applying Lemma B.3 gives

$$\mathbb{P}(\|N\| \geq r) \leq C_1 e^{-C_2 \frac{r^2}{\sigma^2}}, \quad (3)$$

with $C_1 = 2^{\frac{(d-m)}{2}}$ and $C_2 = \frac{1}{4}$.

Combining the above inequalities gives

$$\text{TV}_{\mathcal{M}}(\tilde{p}_\sigma, p_0) \leq C_1 e^{-C_2 \frac{r^2}{\sigma^2}}.$$

□

Proof of Corollary 4.7. By definition of the pointwise reach, for any $n \in N_z \mathcal{M}$ with $\|n\| < \tau(z)$, we have $\Pi(z + n) = z$. Remark that the pointwise reach tune is larger than or equal to the global reach tube. Hence,

$$\text{dist}(z, \Pi(z + n)) \mathbb{1}_{\{\|N\| < \tau(z)\}} = 0.$$

Therefore, we may define an expected pointwise displacement $D_\sigma(z)$ as

$$D_\sigma(z) = \mathbb{E}[\text{dist}(z, \Pi(z + n))] \leq 2\mathbb{E}[\|N\| \mathbb{1}_{\{\|N\| \geq \tau(z)\}}], \quad (4)$$

where the inequality follows from the triangle inequality and z being a candidate point on \mathcal{M} :

$$\text{dist}(z, \Pi(z+n)) = \|\Pi(z) - \Pi(z+N)\| \leq \|z - (z+N)\| + \|(z+N) - \Pi(z+N)\| \leq 2\|N\|.$$

To bound the tail expectation, we again use the Gaussian tail estimate from Lemma B.3. We have $\mathbb{E}\|N\|^2 = \sigma^2 k$, and by Cauchy-Schwarz,

$$\mathbb{E} [\|N\| \mathbb{1}_{\{\|N\| \geq \tau(z)\}}] \leq (\mathbb{E}\|N\|^2)^{\frac{1}{2}} \mathbb{P}(\|N\| \geq \tau(z))^{\frac{1}{2}} \leq \sigma\sqrt{k} \mathbb{P}(\|N\| \geq \tau(z))^{\frac{1}{2}}. \quad (5)$$

By Equation (3), applied with $r = \tau(z)$, Lemma B.3 gives

$$\mathbb{P}(\|N\| \geq \tau(z)) \leq C_1 e^{-C_2 \frac{\tau(z)^2}{\sigma^2}}.$$

Substituting this into Equation (5), we obtain

$$\mathbb{E} [\|N\| \mathbb{1}_{\{\|N\| \geq \tau(z)\}}] \leq \sigma\sqrt{k} \left[C_1 e^{-C_2 \frac{\tau(z)^2}{\sigma^2}} \right]^{\frac{1}{2}}.$$

Combining this with (4) yields the pointwise bound

$$D_\sigma(z) \leq 2\sigma\sqrt{k} \left[C_1 e^{-C_2 \frac{\tau(z)^2}{\sigma^2}} \right]^{\frac{1}{2}}.$$

To obtain the integrated inequality, note that the nearest-point projection is L -Lipschitz on the pointwise reach tube, and therefore a pointwise displacement D_σ induces an $LD_\sigma(z)$ deviation in densities after pushforward along Π . Integrating over \mathcal{M} gives

$$\int_{\mathcal{M}} |\tilde{p}_\sigma(y) - p_0(y)| d\mathcal{H}^m(y) \leq 2L\sigma C_1 \int_{\mathcal{M}} e^{-C_2 \frac{\tau(z)^2}{\sigma^2}} d\mathcal{H}^m(z).$$

□

C. Experimental Setup

In this section, we provide more rigorous experimental details.

For all tasks, we use an Adam optimizer with a learning rate of 10^{-4} . Gradients are clipped at maximum norms of 1.0, as is common in diffusion model training. We also uniformly set $T = 250$ across all diffusion model approaches. All experiments are done on NVIDIA A100 GPUs. We use a simple linear noise schedule with variances increasing from 0.0001 to 0.02, as in (Ho et al., 2020). For all tasks, a fixed number of samples are generated, and invalid samples such as those with NaN/Inf values are discarded before evaluation metrics are computed. In general, discarded samples make up usually no more than 10 out of $\mathcal{O}(10^4)$ samples, minimally affecting the reported results.

For PDM, the paper introducing the approach uses projections of scores. We project scores as approximated through the learned ε outputs. For PIDM, we estimate intermediate samples during training as $\hat{x}_0 = \mathbb{E}[x_0|x_t]$ using standard DDPM sampling.

We encountered several challenges and roadblocks implementing and accurately reproducing the results in RSGMs (Bortoli et al., 2022) due to out-of-date package versions and irreproducible environments. Reproducibility of the RSGM code is a documented issue. A concerted, good-faith effort was made to accurately implement the RSGM code, but ultimately yielded poor results with incompatibilities that would have been a perhaps unfair comparison. In any case, one can infer from the RSGM paper how many nontrivial computations are involved in both training and sampling. This may certainly be desirable for mathematical reasons, but can be non-trivially computationally prohibitive, as is noted by the RSGM authors themselves: a large part of the RSGM paper is focused on efficient techniques for reducing the computational cost of the many manifold-aware steps involved during both training and sampling. Due to these known reproducibility challenges and the unfairness of a comparison against a tailored intrinsic technique with high computational needs, we elect not to include it, or Riemannian Continuous Normalizing Flows (Huang et al., 2022), as one of the comparison techniques in this work.

For the time embedding, we use concatenation of input samples with a predetermined time embedding. We use a simple normalization of the input time for the simpler tasks: in other words, the timestep t is normalized to be between $[0, 1]$ by taking $t_{\text{normalized}} = \frac{t}{T}$, and concatenating the noised sample x_t with $t_{\text{normalized}}$ upon input to the diffusion model.

For each task, unless otherwise noted, the model parameterization (diffusion model or NF) and training-related hyperparameters are kept constant across all techniques to ensure a fair comparison. All NF approaches are run with learning rates of 10^{-4} , batch sizes of 128, and a total number of 40 epochs during training. We use hidden dimensions of 64 for Glow along with the default architecture and [64, 64, 64] for the RealNVP architecture. For better insight into the neural network parameterized models used in each approach, we also report total parameter counts for each technique.

For the generation of uncertainty bands in Figures 3 and 6, we use 10 sampling trials per σ for all experiments. In Figure 7, we use 3 trials per $(\sigma, \# \text{training samples})$ combination.

We note that the intrinsic metrics for the sphere task in Table 1 are computed with a Lambert azimuthal equal-area projection centered at the unit normal pole facing the top of the sphere.

For the mesh task, outliers with norm greater than 2.0 (only present for PIDM and DDPM) were filtered out for histogrammed metrics and visualization. The Gaussian is approximated through heat kernel sampling from a mean node along the geodesics induced by the edges of the shape mesh. The mesh (and thus points on the mesh) are centered at the origin and normalized in an aspect-ratio preserving way such that the maximum distance of a mesh point from the origin is 1.0.

For the protein task, we present results for the PIDM task trained on 300 epochs instead of 1000 epochs for the other techniques due to computational reasons.

	Plane	Sphere	Mesh	Images	Protein
Time embedding	Normalized	Normalized	Normalized	MLP	MLP
Time emb. dim.	1	1	1	64	16
# Training samples	100,000	100,000	100,000	10,000	20,000
Batch size	64	64	64	32	32
Epochs	200	200	200	1000	1000
Hidden dimension	64	64	128	1024	1024

Table 6. Combined diffusion model training configurations for all tasks.

# Parameters	Plane	Sphere	Mesh	Images	Protein
RealNVP	42,738	42,738	—	—	—
Glow	53,010	53,010	—	—	—
DDPM	4,675	4,675	17,539	1,088,769	112,353

Table 7. Total number of trainable parameters for each model across all tasks.

D. Evaluation Metrics

D.1. Point Cloud Evaluation Metrics

We present definitions of all metrics used in Section 5.

Definition D.1 (Coverage). Let $\{x_i\}_{i=1}^n$ denote the set of real samples and $\{y_j^n\}_{j=1}^m$ denote the set of generated samples. For each x_i , let r_i be the distance to its k -th nearest neighbor among real samples $\{x_l\}_{l=1}^n$ and compute the distance to the nearest y_j :

$$d_i = \min_{1 \leq j \leq m} \|x_i - y_j\|_2.$$

We say that a real sample x_j is *covered* if $d_i \leq r_i$. Then, we define the coverage metric as the fraction of real samples that are covered:

$$\text{COV}(X, Y) = \frac{1}{n} \sum_{i=1}^n \mathbb{1}_{d_i \leq r_i}.$$

For the empirical JSD and TVD metrics, we bin samples into histograms, where the number of bins in each axis is fixed for each approach. For the plane and sphere tasks, we use 25 bins in each direction. For the mesh task, we use 50 bins.

D.2. Image Evaluation Metrics

Successfully evaluating distributions of structured images in such a way that avoids the pitfalls of high dimensionality and respects invariances is a known challenge (Jayasumana et al., 2024; Benny et al., 2021). To combat this, many works in image generation employ embedding-based distances, wherein a secondary classification model is trained (or a benchmark model is reloaded) and latent embeddings are extracted from intermediate layers to be used as lower-dimensional embeddings of the input data samples. The Fréchet Inception Distance (FID) score (Heusel et al., 2017) is one example of this, where distances between image distributions are evaluated by studying statistics of the embeddings from the popular Inception-V3 architecture. The idea is that a well-trained model will have learned embeddings which capture image invariances and essential structure, enabling the statistics of such embeddings to act as useful proxies for the data distribution.

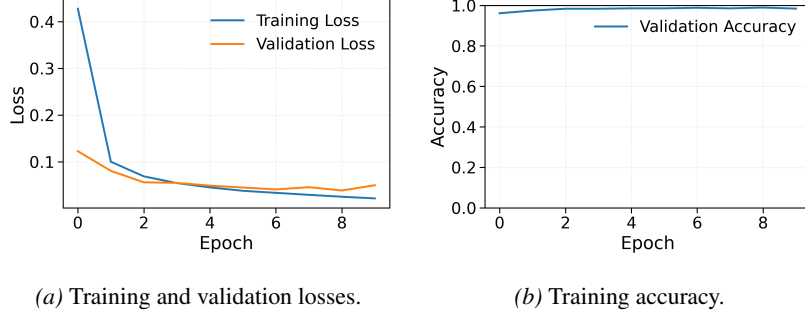
For the MNIST benchmark dataset, the issue of image classification is widely considered to be a solved problem in modern machine learning. To that end, we train a straightforward LeNet-style classifier (Lecun et al., 1998) with 50,190 learnable parameters using a 90%/10% training/validation split over the 60K MNIST training dataset images. After 10 epochs, the model with the best validation loss achieves 98.93% accuracy on the heldout testing dataset of 10K images. The penultimate embeddings are used to compute an FID-like embedding score as follows:

Definition D.2. Define $f_\varphi : \mathbb{R}^{28 \times 28} \rightarrow \mathbb{R}^{28 \times 28}$ as the embedding map, where we let $d = 84$ and define the embedding as the latent vector of the neural network classifier at the penultimate layer. Let $\{x_i\}_{i=1}^N \sim P$ denote true samples and $\{y_j\}_{j=1}^M \sim Q$ denote generated samples. Compute their embeddings $z_i := f_\varphi(x_i)$ and $w_j := f_\varphi(y_j)$ and obtain empirical means and covariances of each collection of embedded samples as $(\hat{\mu}_P, \hat{\Sigma}_P)$ for the true samples and $(\hat{\mu}_Q, \hat{\Sigma}_Q)$ for the generated samples.

From these empirical means and covariances, we compute an FID-like score by computing the Fréchet distance between the empirical Gaussians:

$$\text{FID}_f(P, Q) := \|\hat{\mu}_P - \hat{\mu}_Q\|_2^2 + \text{Tr} \left(\hat{\Sigma}_P - \hat{\Sigma}_Q - 2 \left(\hat{\Sigma}_P \hat{\Sigma}_Q \right)^{\frac{1}{2}} \right). \quad (6)$$

The metrics we report in Section 5.4 are using the FID_f score between the heldout MNIST test set and 1,000 generated samples.



(a) Training and validation losses.

(b) Training accuracy.

Figure 9. Training and validation losses and accuracy for MNIST classifier.

An advantage of the image generation task under fixed total flux case is its easy visual interpretability. We present several samples from each generated image distribution in Appendix G to be analyzed in conjunction with the learned embedding metrics.

The standard MNIST dataset also provides balanced classes, with roughly 10% of all data samples allocated to each digit class. Therefore, one would naturally expect that a well-trained generative model would also have similar class distribution. Again, we utilize the above trained classification model to identify class labels for all generated samples from each generated distribution, and interpret the class distributions of the generated samples against those of the underlying distribution as a measure of distributional accuracy.

Definition D.3 (Class JSD). Define the trained MNIST classifier as $g : \mathbb{R}^{784} \rightarrow \{0, 1, 2, 3, 4, 5, 6, 7, 8, 9\}$. Compute predicted class labels for a set of generated samples $\{x_i\}_{i=1}^N$ as $\hat{y}_i = g(x_i)$. This forms an empirical class distribution $\hat{p}_k^{\text{emp. class}} := \frac{1}{N} \sum_{i=1}^N \mathbb{1}_{\{\hat{y}_i=k\}}$ for $k \in \{0, 1, 2, 3, 4, 5, 6, 7, 8, 9\}$. Let the class distribution of the data be $p^{\text{data class}}$. Then, we report the *class JSD* as the JSD between $\hat{p}^{\text{emp. class}}$ and $p^{\text{data class}}$.

We note, however, that this evaluation metric is inherently hindered by the classification model's inability to determine out-of-distribution samples, as illegible generated samples will still receive a class label. We again recommend the reader to look at these metrics in conjunction with the image examples in Appendix G.

D.3. Protein Evaluation Metrics

Each protein sample has dimensionality $x \in \mathbb{R}^{90}$. As in the image case, this dimensionality hinders the effective usage of histogramming-based evaluation metrics. We present alternative metrics intended to measure the diversity

Definition D.4 (Pairwise RMSD). Denote $\{x_i\}_i^n$ as a set of generated protein backbone samples, for which each sample $x_i = \text{vec}(X_i)$ where $X_i \in \mathbb{R}^{3N}$ contains the coordinates of N atoms, and pick any pair (i, j) with $i \neq j$. Let the root-mean-square deviation (RMSD) between samples x_i and x_j after optimal rigid alignment be

$$\text{RMSD}(x_i, x_j) := \min_{R \in \text{SO}(3), K \in \mathbb{R}^3} \left(\frac{1}{N} \sum_{n=1}^N \left\| X_i^n - (RX_j^{(n)} + K) \right\|_2^2 \right), \quad (7)$$

where R and K are a rotation and a translation, respectively, which are obtained using the Kabsch algorithm. We define the *pairwise RMSD distribution* of the set of generated samples as the collection of all RMSD values over all possible unordered pairs. For the pairwise RMSD metrics presented in Section 5.5, we report the median over the pairwise RMSD distribution. Higher values suggest greater diversity of structures within the collection of generated samples. Lower values suggest possible mode collapse.

Definition D.5 (Maximum Mean Discrepancy). We use the Maximum Mean Discrepancy (MMD) metric, which compares distributions using kernel mean embeddings in a Reproducing Kernel Hilbert Space (RKHS). We present the squared MMD with a Radial Basis Function (RBF) kernel:

$$\hat{\text{MMD}} = \frac{1}{N^2} \sum_{i, i'} k(x_i, x_{i'}) + \frac{1}{M^2} \sum_{j, j'} k(y_j, y_{j'}) - \frac{2}{NM} \sum_{i, j} k(x_i, y_j).$$

In our results, we use a bandwidth of 1.0.

E. Sampling Stability

In this section, we present the same results as in Figure 2 for the remaining tasks (mesh, image, and protein backbone). This empirically demonstrates the known issue of score explosion for diffusion model sampling on manifolds (Bortoli, 2023) and log-determinant explosion for normalizing flows and demonstrates how our proposed approach combats these issues. We remark that samples leading to NaN outputs were removed from tracking. However, they are included in the following section regarding the number of observed NaN/Inf samples associated with each method.

In particular, we frequently observe a continuous reduction in the median magnitude of scores as σ increases.¹ This is expected, as σ increasing means that the nonzero region of p_σ occupies an increasingly larger space in \mathbb{R}^d . We use median aggregation of scores instead of average aggregation of scores in order to avoid outliers biasing the results.

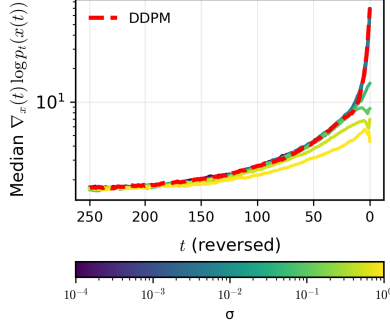


Figure 10. Mesh

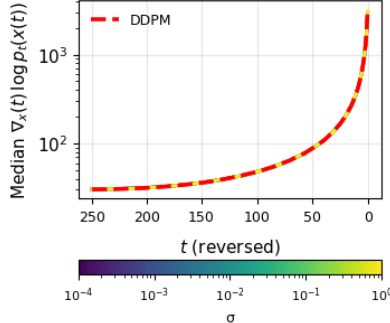


Figure 11. Image

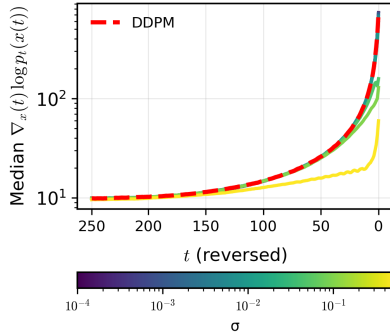


Figure 12. Protein

¹We do not claim that larger scores are inherently “bad.” However, larger scores run the risk of numerical instability or overflow on low-precision training or sampling, the latter of which is growing increasingly common in generative AI applications. Therefore, obtaining competitive performance with bounded scores (as is offered by our proposed p_σ approach) is highly desirable.

F. Manifold Implementations

F.1. Plane Constraint

For the plane task, the manifold is simply an affine subspace

$$\mathcal{M}_{\text{plane}} = \{x \in \mathbb{R}^3 : Ax = b\},$$

where $A \in \mathbb{R}^{1 \times 3}$ is a row vector normal to the plane and $b \in \mathbb{R}$ is an offset. The nearest-point projection map $\Pi(x)$ has a closed form:

Algorithm 2 Nearest-Point Projection onto $\mathcal{M}_{\text{plane}}$

Require: Query point $x \in \mathbb{R}^3$, row vector A , offset b
 1: Compute projection matrix $P = A^\top (AA^\top)^{-1}A$
 2: Compute offset $o = A^\top (AA^\top)^{-1}b$
 3: **Return:** $\Pi(x) = (I - P)x + o$

This expression is exact and requires only a pseudoinverse of AA^\top .

F.2. Sphere Constraint

For the sphere task, the manifold is a quadratic surface

$$\mathcal{M}_{\text{sphere}} = \{x \in \mathbb{R}^3 : \|x - c\|_2 = r\},$$

where $c \in \mathbb{R}^3$ is the center and $r > 0$ the radius. The projection map $\Pi(x)$ rescales the radial direction:

Algorithm 3 Nearest-Point Projection onto $\mathcal{M}_{\text{plane}}$

Require: Query point $x \in \mathbb{R}^3$, sphere center c , radius r
 1: Compute direction $d = x - c$
 2: Normalize direction $u = \frac{d}{\|d\|_2}$
 3: **Return:** $\Pi(x) = c + ru$

This projection is also exact, as each point is simply snapped radially onto the sphere surface.

F.3. Mesh

Define the manifold as

$$\mathcal{M}_{\text{mesh}} = \{x \in \mathbb{R}^3 : h(x) = 0\},$$

where $h(x)$ is the level set defining the surface of the mesh. We implement an approximate nearest-point projection map $\Pi(x)$:

Algorithm 4 Nearest-Point Projection onto $\mathcal{M}_{\text{mesh}}$

Require: Query point $x \in \mathbb{R}^3$, mesh \mathcal{T} with vertices V and faces F

- 1: Compute k nearest vertices $v_1, \dots, v_k \in V$
- 2: Gather incident faces for each v_i
- 3: Rank candidate faces by distance from x to their centroids
- 4: keep closest m faces
- 5: **for** each candidate triangle τ_j with vertices (a, b, c) **do**
- 6: Compute closest point y_j on τ_j using an exact point-triangle projection
- 7: Record $d_j^2 = \|x - y_j\|^2$
- 8: **end for**
- 9: Let $j^* = \arg \min_j d_j^2$
- 10: **Return:** $\Pi(x) = y_{j^*}$

This procedure guarantees that $\Pi(x)$ lies on $\mathcal{M}_{\text{mesh}}$. The parameters k and m trade off accuracy and cost: larger values increase the candidate pool size and robustness, while smaller values reduce the computational needs. In all of our experiments, we use $k = 4$ and $m = 32$.

F.4. Images

We construct a variant of the MNIST dataset constrained by total image flux by embedding each image into the manifold

$$\mathcal{M}_{\text{flux}} = \{x \in \mathbb{R}^{784} : \mathbf{1}^\top x = s\},$$

where $\mathbf{1} \in \mathbb{R}^{784}$ is a vector of all ones and $s \in \mathbb{R}$ is the total pixel sum. The constraint Jacobian may be written as

$$J_g(x) = \nabla h(x)^\top = \mathbf{1}^\top \in \mathbb{R}^{1 \times 784}, h(x) = \mathbf{1}^\top x - s,$$

constructing tangent and normal spaces

$$T_x \mathcal{M} = \{v \in \mathbb{R}^{784} : \mathbf{1}^\top v = 0\}, N_x \mathcal{M} = \text{span}\{\mathbf{1}\},$$

with the unit normal vector $\hat{n} = \frac{1}{\sqrt{784}} = \frac{1}{28}$. The orthogonal projector onto $T_x \mathcal{M}$ may be written as

$$P_T = I - \frac{1}{784} \mathbf{1} \mathbf{1}^\top$$

and the orthogonal projector onto $N_x \mathcal{M}$ is

$$P_N = \frac{1}{784} \mathbf{1} \mathbf{1}^\top.$$

Samples from p_σ may be formed by perturbing each sample from p_0 with Gaussian noise along the normal direction:

$$x_\sigma^i = x_0^i + \frac{\varepsilon}{28} \mathbf{1}.$$

We may write the nearest-point projection onto $\mathcal{M}_{\text{flux}}$ as

$$\Pi(x) = \arg \min_{y \in \mathcal{M}} \frac{1}{2} \|y - x\|^2 = x + \frac{s - \sum_{i=1}^{784} x[i]}{784} \mathbf{1} = \left(I - \frac{1}{784} \mathbf{1} \mathbf{1}^\top \right) x + \frac{s}{784} \mathbf{1}.$$

F.5. Protein Generation Problem

Let $x_{i,a} \in \mathbb{R}^3$ denote the coordinates of atom $a \in \{\text{N, CA, C}\}$ in residue i .

We impose two types of local geometric constraints for the purposes of this task: bond length constraints and bond angle constraints.

Let \mathcal{E}_{len} and \mathcal{E}_{ang} denote the index sets for bond length (pairs of atoms) and bond angle (triplets of atoms) constraints, respectively. For each $e = ((i, a), (j, b)) \in \mathcal{E}_{\text{len}}$ construct the bond length residual as

$$r_e(x) = \|x_{i,a} - x_{j,b}\|_2 - \ell_{ab},$$

where ℓ_{ab} is the bond length constraint for the atoms indexed by a and b . For each $e = ((i, a), (j, b), (k, c)) \in \mathcal{E}_{\text{ang}}$, construct the bond angle residual as

$$r_e(x) = \cos \theta_e(x) - \cos \theta_e^*, \cos \theta_e(x) = \frac{(x_{i,a} - x_{j,b}) \cdot (x_{k,c} - x_{j,b})}{\|x_{i,a} - x_{j,b}\|_2 \|x_{k,c} - x_{j,b}\|_2}.$$

Collecting all such bond length and bond angle residuals gives

$$c(x) = (r_e(x))_{e \in \mathcal{E}_{\text{len}} \cup \mathcal{E}_{\text{ang}}}.$$

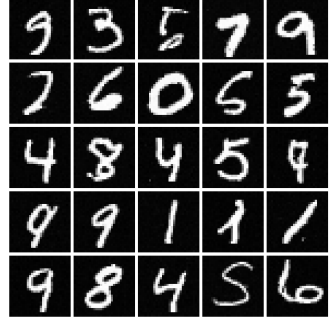
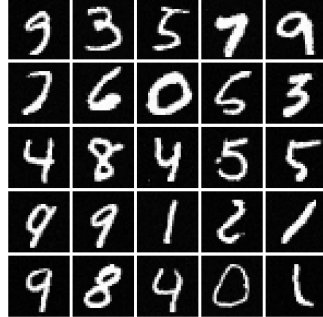
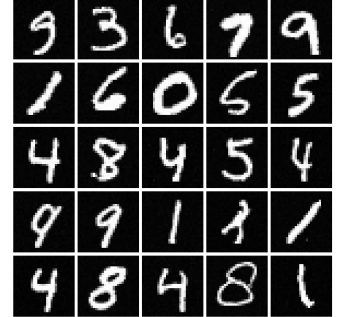
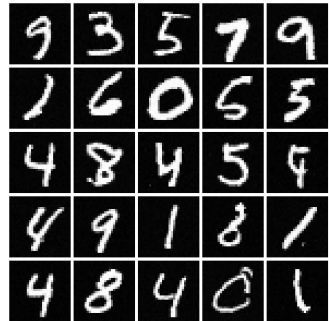
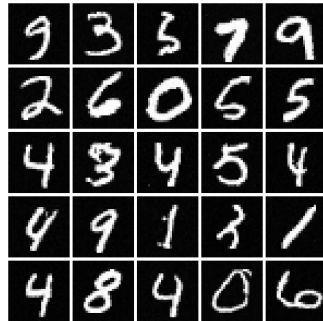
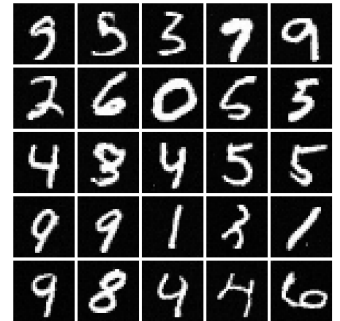
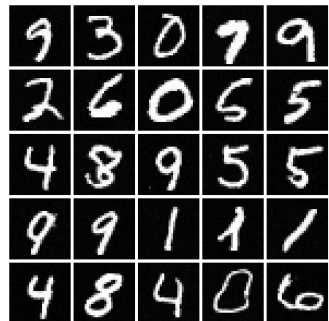
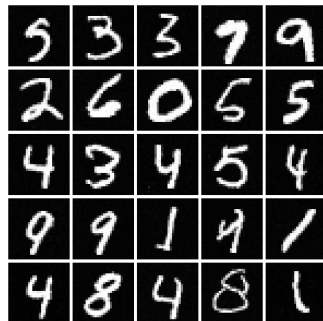
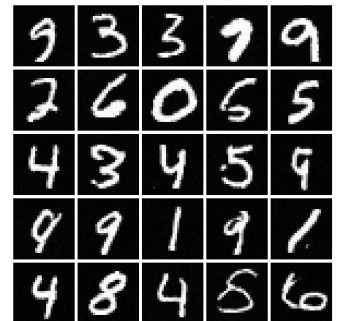
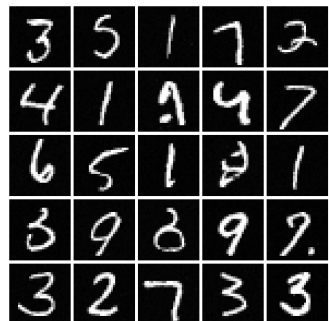
The protein backbone constraint manifold is thus the zero level set

$$\mathcal{M}_{\text{protein}} = \{x \in \mathbb{R}^D : c(x) = 0\}.$$

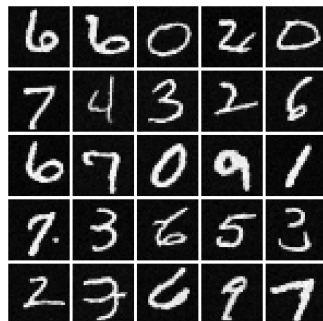
To project samples to $\mathcal{M}_{\text{protein}}$, we use a Gauss-Newton optimization algorithm with a maximum number of 5 iterations, a step size of 1.0, a damping factor of 10^{-4} , and a tolerance maximum residual of 10^{-4} .

G. Images with Total Flux Samples

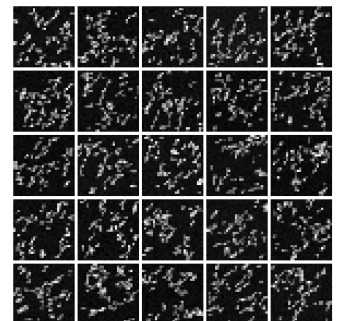
We present additional sample images from each generated distribution at various training data sample set sizes and σ to provide improved qualitative insight into the sample quality from each learned distribution, complementing the quantitative metrics presented in Section 5.4.

(a) $\sigma = 0.0001$ (b) $\sigma = 0.0005$ (c) $\sigma = 0.001$ (d) $\sigma = 0.005$ (e) $\sigma = 0.01$ (f) $\sigma = 0.05$ (g) $\sigma = 0.1$ (h) $\sigma = 0.5$ (i) $\sigma = 1.0$ 

(j) DDPM

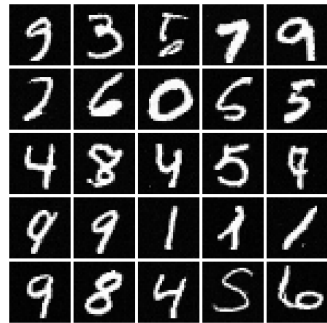
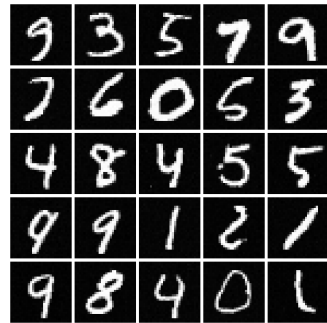
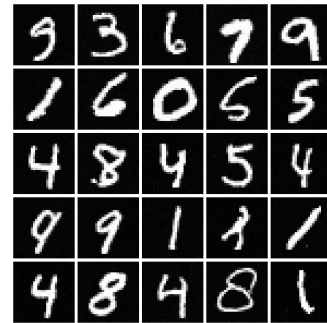
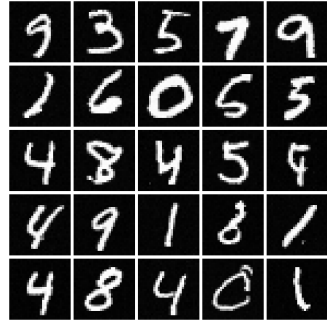
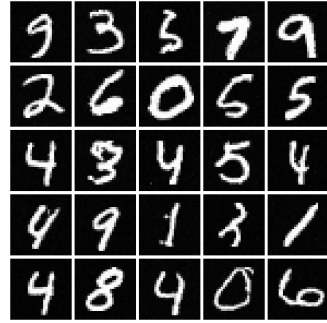
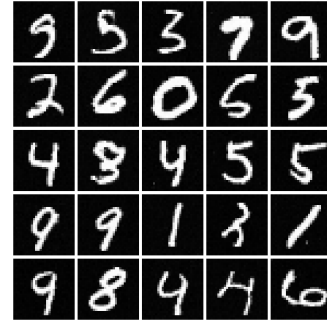
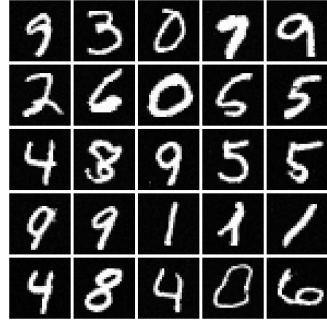
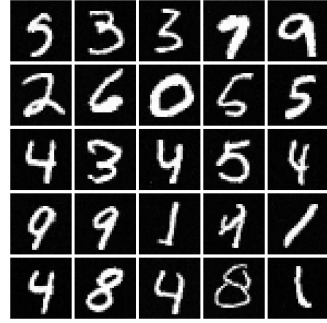
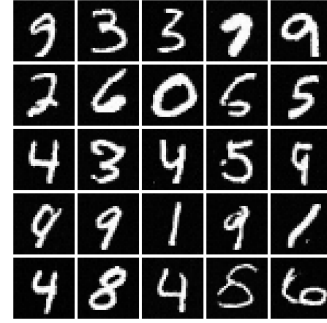
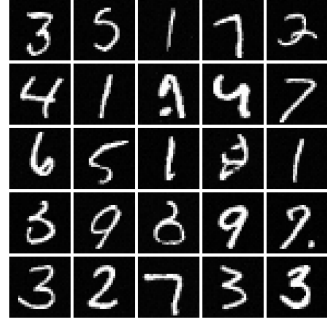


(k) PIDM

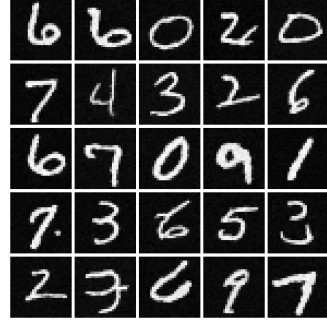


(l) PDM

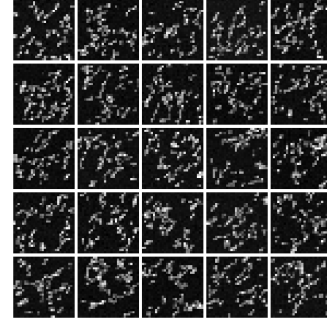
Figure 13. Examples of effect of σ with 100 training data samples.

(a) $\sigma = 0.0001$ (b) $\sigma = 0.0005$ (c) $\sigma = 0.001$ (d) $\sigma = 0.005$ (e) $\sigma = 0.01$ (f) $\sigma = 0.05$ (g) $\sigma = 0.1$ (h) $\sigma = 0.5$ (i) $\sigma = 1.0$ 

(j) DDPM

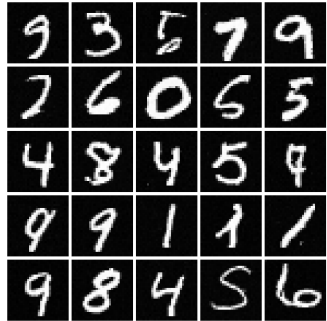
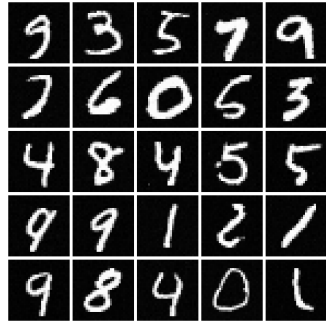
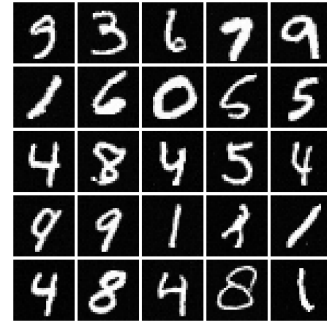
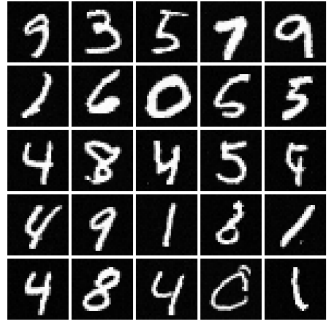
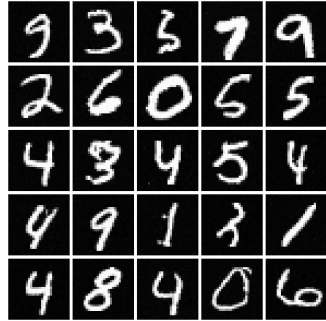
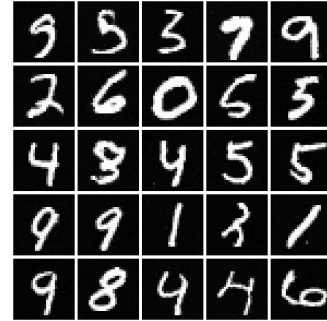
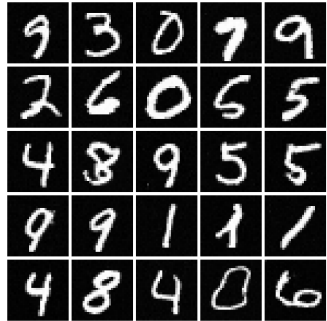
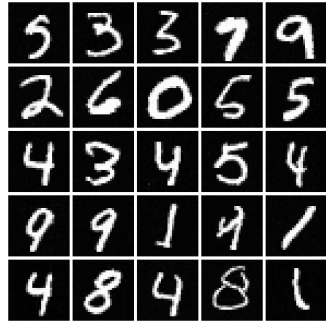
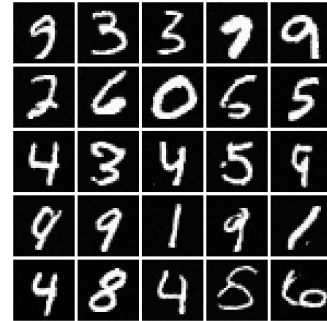
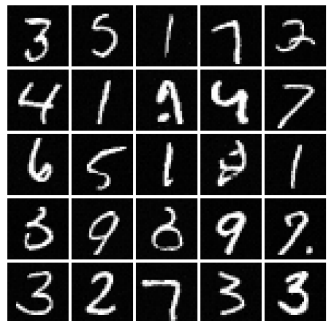


(k) PIDM

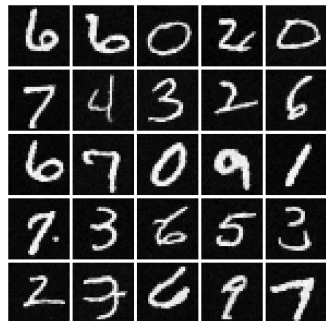


(l) PDM

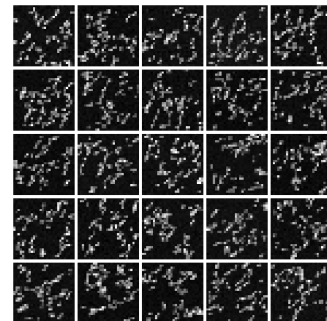
Figure 14. Examples of effect of σ with 1,000 training data samples.

(a) $\sigma = 0.0001$ (b) $\sigma = 0.0005$ (c) $\sigma = 0.001$ (d) $\sigma = 0.005$ (e) $\sigma = 0.01$ (f) $\sigma = 0.05$ (g) $\sigma = 0.1$ (h) $\sigma = 0.5$ (i) $\sigma = 1.0$ 

(j) DDPM



(k) PIDM



(l) PDM

Figure 15. Examples of effect of σ with 10,000 training data samples.